

SUB-BASALT CONVERTED-WAVE IMAGING – OFFSHORE WEST IRELAND¹

Alexander Droujinine¹, Steve Buckner² and Ross Cameron²

¹British Geological Survey (now at Shell International Exploration & Production B.V., Kessler Park 1, 2288 GS Rijswijk, The Netherlands, E-mail: Alexander.Droujinine@shell.com)

²Marathon International Petroleum (GB) Ltd., Marathon House, Rubislaw Hill, Anderson Drive, Aberdeen AB2 4AZ, UK

¹ Paper presented at the 67th EAGE Conference & Exhibition, Madrid, Spain, 13-16 June 2005

ABSTRACT

High-velocity volcanic units that overlay lower velocity structures hinder exploration in potential hydrocarbon producing areas adjacent to the Corrib Field, offshore West Ireland. A recent 3D seismic reflection dataset acquired in the NW Corrib region is used to map major volcanic units and a heavily faulted sub-volcanic structure. The low frequency content of the seismic data is taken into account in the acquisition design. A case study is conducted to demonstrate how wave mode dependent data pre-processing, velocity analysis and 3D prestack imaging techniques should be integrated for the purpose of producing enhanced depth images of the target zone when compared to conventional PP processing. We show that the mode-converted waves of type PSPPSP provide a better image of the sub-basalt structures than the PP waves. Separation of wave modes in a pre-processing step is crucial for imaging these different wave modes separately. For carrying out the total velocity model building workflow, a priori knowledge on the area in terms of the different geologic layers and their geophysical parameters is very important.

Keywords: Sub-basalt imaging, converted waves, GDRT, NW Corrib.

INTRODUCTION

The interpretation of seismic data acquired in basalt-covered areas is often challenging due to the presence of high-velocity layers. A large number of field and laboratory experiments illustrate the variability in aggregate thickness (from tens to several thousands meters) and elastic properties of these layers at a variety of scales (Planke et al., 1999). A high impedance contrast between the top-basalt (TB), the base-basalt (BB) boundaries and the surrounding sediments is known to generate strong multiples (free-surface multiples, inter-basalt peg-legs, etc.) and reduces the P-wave penetration (Spitzer et al., 2003). Weak sub-basalt reflections suffer severe loss in frequency content due to a combination of scattering effects and intrinsic attenuation (Maresh and White, 2005). Sub-basalt PP reflections are often swamped by mode conversions at the basalt-sediment interface (Purnell, 1992; Barzaghi et al., 2002). These are proving to be major problems for seismic imaging in the North Atlantic margin, from Norway to Ireland.

Marine streamer data at moderate offsets of less than 6 km can be reprocessed using advanced noise attenuation techniques specifically designed to reduce uncertainties of short-wavelength velocity perturbations (Ogilvie et al., 2001). In this case, non-PP or mode conversions often cause degradation of seismic sections and should be deconvolved. On the other hand, a straightforward single-step prestack time migration (PSTM) or prestack depth migration (PSDM) combining all modes (events) is usually not reliable because events migrated with inadequate combinations of velocities produce severe migration artefacts due to frequency dependent event coupling. Since distortion is expected to be limited for data characterized by a single event, a domain transform or wave-equation complete wavefield separation is usually required to minimize cross-talk energy between individual events (Dillon et al., 1988). In practice, interference between various events on prestack gathers always prevents the desired clear separation of events (Spitzer et al., 2003).

To facilitate event-oriented data pre-conditioning and to accomplish event selection during the migration process, we invoked the decoupled prestack migration formula (Droujinine, 2005). According to the elastic migration principle (Dillon et al., 1988), we migrated data using a combination of velocities and event enhancement amplitude weights suitable for each event. This makes it possible to avoid misprocessing and misinterpreting non-PP arrivals as primary PP reflections, without applying labour-intensive pre-processing that involves the use of handpicked mutes or interactive interpretations based on calculations of the traveltimes response (Barzaghi et al., 2002). In event-based migration with accurate velocities, migrated energy from assumed wave-propagation modes coincides with the actual reflector, although different parts of this reflector are imaged with each event.

The aim of the present case study is to apply the above approach to a recent 3D seismic reflection dataset acquired in the NW Corrib region, offshore West Ireland (Figure 1). The area is approximately 154 km² (20×7.7 km) of 60 fold data acquired by Veritas DGC in 2002 using a 6 km hydrophone receiver cable (see Table 1). The objective is to demonstrate how wave mode dependent data pre-processing, velocity analysis and 3D prestack imaging techniques should be integrated for the purpose of producing enhanced depth images of the target zone when compared to conventional processing. Pre-processed data have typical problems in basalt-covered areas: poor PP signal and strong coherent noise represented by multiples and converted waves. Referring to previous modelling studies (Purnell, 1992; Planke et al., 1999; Spitzer et al., 2003), it is envisaged that 6 km offsets, spatial sampling within the Nyquist limit and 12 m source depth may be sufficient to observe non-aliased basalt-related converted waves.

GEOLOGICAL BACKGROUND

Ireland's extensive offshore territory is considered one of the most promising petroleum hydrocarbon exploration territories in Europe. The current level of exploration interest in

Irish waters is likely to be maintained and future growth is expected, particularly in the Atlantic Frontier. The Atlantic Frontier presents the offshore industry with an opportunity to test new deepwater technology. The NW Corrib area (Figure 1) is located in the Slyne-Erris Basin that is composed of a series of Mesozoic half-grabens of alternating polarity. The Slyne-Erris Basin is one of a number of basins on the NE Atlantic margin that have experienced a multi-phase extensional and exhumation history during the late Paleozoic to Cenozoic period (see Silva and Corcoran, 2002, and references cited therein). The main exploration targets in the basin are the Middle Jurassic and Triassic sandstones, similar to the Sherwood Sandstone and Mercia Mudstone Formations of the East Irish Sea Basin; the Jurassic is overlain unconformably by a Cretaceous sandstone-chalk sequence, Tertiary basalt lava flows, and capped by Tertiary/Quaternary sands and muds (Dancer, 2002; Dancer et al. 2005). The primary hydrocarbon play in this basin consists of a Lower Triassic sandstone reservoir in structural traps, sealed by Upper Triassic evaporites and mudstones. The hydrocarbon potential of the region has been illustrated by the Corrib 18/20-1 gas field discovery by Enterprise Oil in the Slyne Trough off County Mayo. This discovery increases the possibility that Carboniferous coal measures also have source potential in the region. The field, which has 1TCF of dry gas reserves, is currently undergoing development by Shell, Statoil and Marathon that has resulted in the drilling of six exploration/development wells. The infrastructure of the Corrib field could significantly reduce the development cost of any further commercial discoveries in the vicinity. Despite this discovery, the structural history of the basin remains poorly understood. Previous imaging tests (Silva and Corcoran, 2002; Dancer, 2002) show only fair image quality due to the presence of near-surface volcanic units and a heavily faulted sub-volcanic structure.

SEISMIC ACQUISITION

The survey is located in the license block 3/94 offshore NW Ireland (Figure 1). Some acquisition parameters are listed in Table 1. This acquisition eliminates some problems (fold, cable length, etc.) related to the previous 3D survey acquired in 1997 by Western Geophysical. The 800 Gb A-1483 dataset is divided into five subsets, as shown in Figure 1. The test site (subsets 3 and 4) incorporates the 60-fold data with the highest signal-to-noise ratio and is covering approximately 154 km² (20×7.7 km).

PROCESSING RESULTS

The five essential phases of our sequential wave mode dependent processing flow are as follows: (1) initial signal enhancement done by CGGV (signature processing, multi-step multiple attenuation, etc.); (2) wavefield separation based on the data-driven or attribute-based Generalized Discrete Radon Transform (GDRT) algorithm (Droujinine, 2005); (3) iterative 3D PSTM followed by velocity model building (Yilmaz, 2001; Robein and Hanitzsch, 2001); (4) zero-offset (ZO) time-to-depth mapping and subsequent depth model updates using results of phase 3; (5) iterative 3D PSDM using results of phase 4.

Phase 1: Signal Enhancement

The objective of phase 1 was to produce a set of pre-processed shot point gathers ready to use in multi-wave-type imaging. The quality of the original data was rather poor due to the noise that masked primary events. Therefore, the following processing sequence was applied: reformatting, seismic-navigation merge, deterministic zero phasing and de-bubbling using the recorded source signature, a low cut 3 Hz / 18 dB per octave filter that keeps low frequency data, swell noise attenuation, inverse Q -filtering, and multi-step multiple attenuation that includes refracted T-K multiple attenuation with a cut-off velocity of 2200 m/s, the single-pass Surface Related Multiple Elimination (SRME) using half of the cable

length for multiple model creation and subtraction of predicted multiples using 1/3 of the cable length (Verschuur and Berkhout, 1997), and diffracted multiple attenuation based on spectral discrepancy between multiples and primaries (Hugonnet et al., 2004). Figure 2a shows a common-shot gather (subset 4) after phase 1: some remaining low frequency noise can be observed on long-offset traces. Conventional RMS velocity analysis was carried out on selected groups of gathers for QC purposes (Figure 2b). In Figure 2b, one can observe primary PP waves (A), symmetric converted waves (B) and surface-related multiples (C).

Phase 2: Wavefield Separation

Primaries and multiples can be separated in the Radon domain because of their different RMS velocities (Yilmaz, 2001). Event separation may be enhanced by the linear, parabolic or generalized Radon transform, used to increase the PP-wave signal-to-noise ratio and to identify non-PP events not interpretable on the PP sections. Here, we take the advantage of the attribute-based GDRT that “interprets” seismic data to find dip and curvature attributes of the wave fronts. This is a discrete version of the Generalized Radon Transform (GRT) (Beylkin, 1982) that extends slant-stack data transformations used in seismic processing. A straightforward high-frequency implementation of the GDRT involves weighted summation of deconvolved trace samples $u(t, h)$ along a set of prescribed traveltimes $t = \tau(h)$ expressed in terms of the measurable local attributes $P(h) = \partial\tau(h)/\partial h$ and $Q(h) = 0.5\partial^2\tau(h)/\partial h^2$, where t is the time and h is the appropriate domain variable (offset, angle, etc.). These attributes are determined by representing discretely sampled prestack shot gathers as a superposition of Biondi’s (1992) beam segments whose spectral phase and amplitude functions match instantaneous characteristics or complex-trace attributes of the locally coherent event to be enhanced, migrated or attenuated. In a typical application, traces are stacked along locally parabolic traveltimes segments

$\tau(h) \approx \tau(h_B) + P(h_B)(h - h_B) + Q(h_B)(h - h_B)^2$ (local moveout operators) around certain (reference) value $h = h_B$. In contrast to the classical parabolic Radon transform (Yilmaz, 2001), these segments are local in that they do not extend over the entire $(t-h)$ range (typically, 10-20 traces and 5-7 vertical samples are summed). The procedure is a two-parameter short summation search for locally coherent events by seeking the maxima of some coherency function at each $(t-h)$ -point in the data set. One could think of using this procedure to fill in the entire $(\tau - P - Q)$ space. The basic assumption is that waveforms in the processing window are finite in number. Each is considered to have its own instantaneous phase curvature and direction of arrival. The forward GDRT transformation of the $(t-h)$ data into the $(\tau - P - Q)$ domain allows each event to be selected and enhanced or muted out. The remaining data are then inverse transformed.

Shown in Figure 2a is an example of prestack $(t-h)$ domain gather prior to wavefield separation. It contains the source signals (waveforms), some of which we would like to retrieve (e.g. primary PP reflections in near-offset range and some mode conversions in mid-offset range). The idea of wavefield separation is to filter out the unwanted waveforms and to recover the desired signal that has been corrupted by additive noise, producing the corrupted signal. As with local $(\tau - p)$ methods (Theune et al., 2005), the first pass of GDRT is implemented as follows:

1. Divide the input gather (see the RMS velocity spectrum in Figure 3a) into small $(t-h)$ segments and do the forward GDRT transform for every segment.
2. In the local $(\tau - P - Q)$ domain, we pick the most dominant P and Q values corresponding to strong unwanted events, and inverse transform these values into $(t-h)$ domain. This yields the noise model segment.
3. Subtract the noise model from the input segment in the least-squares sense.

The output gather (see the RMS velocity spectrum in Figure 3b) is obtained by repeating steps 1-3 for all the segments. The second pass of GDRT consists of the following two steps:

1. Divide the enhanced gather (output of pass 1 GDRT) into small ($t-h$) segments and do the forward GDRT transform for every segment.
2. In the local ($\tau-P-Q$) domain, we pick the most dominant P and Q values corresponding to enhanced primary events, and inverse transform these values into ($t-h$) domain. This yields the signal model segment.

The result of repeating steps 1 and 2 for all the segments yields the RMS velocity spectrum shown in Figure 3c (compare with Figure 9 in Planke et al., 1999).

The output of GDRT filtering (Figures 3b and 3c) has the characteristic mixed mode appearance suitable for “predict and then subtract” noise attenuation and multi-wave-type imaging algorithms. The result of GDRT filtering is better than before (compare Figures 3a and 3b,c), although the finite aperture limitation does not allow total suppression of spurious parabolic events having the appearance of water-column multiple diffractions (labelled M in Figure 3b). Assuming that long-period multiples had effectively been attenuated during phase 1, the iterative GDRT gives good enhancement of converted wave modes, as illustrated in Figure 3b. In Figure 3c, the P-wave data after enhancement may be defined as the difference $u_p = u - u_c$, where u is the observed data after multiple attenuation and u_c is the converted-wave PSPPSP (S traveling inside basalts) arrival picked on the semblance panel in Figure 3b. The iterative GDRT (pass 2 in Figure 3c) also suppresses the asymmetric PPSP waves (S propagating upwards and converted to P at the sea floor) from the TB boundary. Remaining water-column multiples can be attenuated by alternative methods such as higher order SRME or a combination of standard Radon demultiple plus simple inner trace mute.

In Figure 4, PP and converted-wave time migrated results (a single line) after GDRT wave-type separation and PP time-to-depth vertical stretching are compared. When compared

with the PP image (Figure 4a), the converted-wave section in Figure 4b offers a well-balanced result: the noise level is reduced and sub-basalt reflectors are better resolved than those in Figure 4a. In Figure 4, it is interesting to see that the artifacts of GDRT and residual multiples were not actually enhanced by PSTM. Also, the image in Figure 4b is of lower frequency content than that in Figure 4a. This supports our statement that low-frequency primaries from within and beneath basalts have been enhanced during the processing phases 1 and 2. Observe an apparent difference in dip of the deeper reflectors at the NW end of the line between Figures 4a and 4b. Since the current time-to-depth conversion did not account for a non-PP propagation history described by the PSPSP code, this difference is a direct consequence of Snell's law: the angle of converted-wave transmission is not equal to the angle of PP-wave transmission. The error of time-to-depth conversion will be eliminated during phase 5.

Phase 3: Time-Domain Model Building

The key step of the time-domain velocity model building is to apply the conventional Dix inversion to the stacking velocity field (Yilmaz, 2001). Due to well-known uncertainties of Dix inversion (Robein and Hanitzsch, 2001), we focused our attention on an approximate match between interpreted interval velocities and sonic logs acquired in the adjacent Corrib field down to 3.8 km. The velocity field was also constrained by the linear regional regression formula of Ogilvie et al. (2001). Even though there are no wells within the study area, the nearest well (18/20-1) is less than 5 km to the east. This makes it possible to correlate previously interpreted horizon markers with the seismic data. Moreover, interpreted top/base maps based on the 1997 Corrib 3D seismic adjacent to the 2002 NW Corrib project (A-1483), can be potentially correlated with key horizons from the study area. In this study,

the initial V_P/V_S values for the basalt and surrounding sediments were based on Christie et al. (2002)*.

Once the P velocity grid had been constructed and the V_P/V_S ratio was defined, the pre-processed subsets 3 and 4 after wavefield separation were migrated several times, using PSTM for PP and PSPPSP wave types identified during phase 2 (Barzaghi et al., 2002). Similar to the Kirchhoff PSTM processing (Yilmaz, 2001; Robein and Hanitzsch, 2001), the GDRT PSTM procedure is divided into two major steps: (1) calculation of traveltimes between normal-ray image points and observation points; (2) using these traveltimes to map the reflections to their true time-domain locations (t_0, ξ) , where t_0 is the normal-ray traveltime and ξ is the acquisition parameter that defines current CDP or common reflecting point (CRP) location. Figure 5 compares this procedure and conventional PSTM. The objective is to emphasize the impact of focusing imposed by PSTM and to pay no attention to errors in locating reflections in their proper position, even though imaging and positioning problems in time processing are often interrelated. The time section in Figure 5a was obtained by PSTM-type focusing of NMO-corrected common midpoint (CMP) traces followed by the RMS velocity semblance analysis. In Figure 5a, amplitude distortion is associated with a dispersion of reflection points, referred to as CMP smearing (Yilmaz, 2001). It is seen that the PSTM section displayed in vertical two-way time in Figure 5b gives better imaging quality than the time section in Figure 5a. Since the GDRT PSTM is based on the local parabolic approximation that overcomes limitations of global hyperbolic moveout (Yilmaz, 2001), the migrated section in Figure 5b shows improvement in continuity and coherency of reflections when compared to the section in Figure 5a.

Finally, the initial velocity model in time (Figure 6) was generated using interpreted time horizons and interval velocities. In areas of poor image quality, the existing

* The paper deals with V_P and V_S in basalts and hyaloclastites in Lopra-1/1A.

interpretation served as a guide for model building. Even though the application of PSTM helped to improve the image of the BB horizon, most sub-volcanic units could not be seen on the migrated gathers in Figure 5b indicating that imaging problems still exist. Therefore, we ran a succession of trial time migrations of moveout-corrected CDP gathers over a range of model parameters to account for remaining lateral velocity variations. The final time-domain velocity model after time-to-depth conversion was then used in PSDM of the surface seismic data.

Phase 4: Depth-Domain Model Updating

Regarding the choice of appropriate time-to-depth mapping, vertical stretching of the velocity grid in Figure 6 was found to be a poor approximation due to laterally varying high-velocity intervals. Instead, the initial depth model was constructed by means of ray-map depth migration of the time model in Figure 6 using interval velocities calculated by the generalized Dix inversion (Droujinine, 2005). This inversion extends RMS velocity transformations (Robein and Hanitzsch, 2001) to laterally varying media. The mapping process is equivalent to the back propagation of zero-offset traces along normal-incidence rays that correctly depth migrate time sections if the input velocity model is sufficiently accurate. Since the initial depth model is never exceptionally accurate, a layer-stripping depth focusing approach is applied to minimize the cumulative error resulting from velocity and depth related errors in the starting model. It is important to achieve optimal depth-domain focusing of the key horizons by starting with the shallow horizons and moving downward.

To verify the correctness of our velocity model, we need to examine the flatness of common image point gathers from the PSDM. Therefore, subsets 3 and 4 were migrated several times during phase 4, using the GDRT depth migration procedure (Droujinine, 2005) related to the fast wavepath or Fresnel-aperture PSDM (Tabti et al., 2004). This procedure was applied to map the reflections to their true vertical depth locations (z, ξ) for both PP and

converted waves. The two key migration steps are as follows: (1) calculation of multi-wave-type traveltimes between the image points (z, ξ) and observation points; (2) using these traveltimes to map the reflections to the image points. Input data were pre-processed shot gathers after GDRT wavefield separation, followed by traveltime computations in terms of local moveout operators (Biondi, 1992). Figure 7 is an example of vertical prestack depth-migrated PP and PSPPSP sections (top and bottom panels, respectively). Although some diffracted events due to the Fresnel aperture still remain in shallow parts of the image in Figure 7, PSDM provides a sufficiently accurate image of the BB horizon and sub-basalt reflectors. A comparison between PP and converted-wave sections in Figure 7 shows that the PSPPSP PSDM improves the quality of the image particularly for the BB horizon and the continuity of the deeper reflectors. It also yields a better definition of the basalt structure and related faults required for advanced model verification and refinement. Figure 7 demonstrates an excellent match between the reflectors in PP and non-PP images in depth.

Phase 5: Final PSDM

Encouraged by the improvement in depth image quality along test lines, a major 3D PSPPSP PSDM of the pre-processed subsets 3 and 4 was undertaken, resulting in a successful re-interpretation of the structure below the TB horizon (Figure 8). The PSDM algorithm incorporating converted-wave imaging capability allows a reasonably continuous interpretation of all horizons with a rollover anticline structure below the BB horizon (Figure 8). Figure 8 provides a detailed account of the main volcanic sequence. The basalt structure appears to be largely tabular, thickening towards the SE end of the line. It is cut by a series of small grabens or tilted fault blocks. The volcanic units are represented by interbedded volcanics and overall are not massive in thickness. These are regional horizons and as such it is possible that at this location the TB surface is represented by clastics and not volcanics hence the lack of impedance contrast. The resulting depth images allow a confident mapping

of the overburden faults between horizons TB and CR structurally detached from horizons LM and SH. According to Dancer (2002), the Jurassic deposits are overlain unconformably by a Cretaceous sandstone and chalk sequence. It turns out that our stratigraphic interpretation is consistent with the geological model put forward by Dancer et al. (2005). Because of the smooth nature of sediments below the CR horizon, a smooth, constant-gradient velocity analysis at Jurassic/Triassic level can prove beneficial.

DISCUSSION AND CONCLUSIONS

The present case study has shown that converted-wave prestack depth migration combined with wavefield separation during pre-processing is suitable for sub-basalt imaging in the NW Corrib region (offshore the West Coast of the Republic of Ireland). The following aspects of the seismic acquisition were essential to achieve our goals: deep source and receiver positioning in order to enhance the low-frequency response; fine source/receiver spatial sampling within the Nyquist anti-aliasing criterion, and sufficiently large offsets. Careful re-interpretation has proven to be essential, with horizons added or subtracted to the velocity model. Throughout the model building, application of iterative prestack time migration and a clear understanding of geological setting are important in order to constrain the velocity picking. Comparison of the migrated results obtained by using the PP and converted-wave migration methods has substantiated the importance of the P₁PPSP wave, which traveled through the basalt as an S-wave.

ACKNOWLEDGEMENTS

This work was funded by industrial sponsors (BG, BGP, BP, Chevron, ConocoPhillips, CNPC, ENI-Agip, ExxonMobil, GX Technology, Kerr-McGee, Landmark, Marathon, Norsk Hydro, PDVSA, Shell, Schlumberger, Total, and Veritas) at the British Geological Survey

(BGS/NERC). It is published with the permission of Corrib partners (Shell, Statoil and Marathon). Thorough reviews from Phil Christie (Schlumberger) and Eric Verschuur (Delft University of Technology) were helpful in improving the manuscript.

REFERENCES

- Barzaghi, L., Calcagni, M., Passolunghi, M., and Sandroni, S., 2002, Faeroe sub-basalt seismic imaging: a new iterative time processing approach: *First Break*, **20**, 611-617.
- Beylkin, G., 1982. Generalized Radon transform and its application. PhD thesis, New York University, New York.
- Biondi, B., 1992, Velocity estimation by beam stack: *Geophysics*, **57**, 1034-1047.
- Christie, P., Gollifer, I., and Cowper, D., 2002, Borehole seismic results from the Lopra deepening project: *Journal of Conference Abstracts*, **7**, 138-139.
- Dancer, P.N., 2002, The Corrib field – changes in structural interpretation through 2D, 3D and PreSDM seismic data: EAGE 64th Conference – Florence, Italy, 27-30 May, Paper G-33.
- Dancer, D. N., Kenyon-Roberts, S. M., Downe, J. W., Baillie, J. M., Meadows, N. S., and Maguire, K. 2005. The Corrib gas field, offshore west of Ireland. In : Doré, A. G., and Vining, B. A. (eds) *Petroleum Geology: North-West Europe and Global Perspectives—Proceedings of the 6th Petroleum Geology Conference*, pp.1035–1046, Geological Society, London.
- Dillon, P. B., Ahmed, H., Roberts, T., 1988, Migration of mixed mode VSP wavefields: *Geophysical Prospecting*, **36**, 825-846.
- Droujinine, A., 2005, The attribute based generalized discrete Radon transform: *Journal of Seismic Exploration*, **14**, 155-196.

- Hugonnet, P., Hardouin, D., Lecocq, P., 2004, Deepwater case histories - SPME/HR Radon/diffracted multiple attenuation: Data Processing SIG, Houston, 15 September.
- Maresh, J., and White, R.S., 2005, Seeing through a glass, darkly: strategies for imaging through basalt: *First Break*, **23**, 27-33.
- Ogilvie J.S., Crompton R. and Hardy N.M. 2001, Characterization of volcanic units using detailed velocity analysis in the Atlantic Margin, West of Shetlands, United Kingdom: *The Leading Edge*, **20**, 34-50.
- Planke, S., Alvestad, E., and Eldholm, O., 1999, Seismic characteristics of basaltic extrusive and intrusive rocks: *The Leading Edge*, **18**, 342-348.
- Purnell, G. W., 1992, Imaging beneath a high-velocity layer using converted waves: *Geophysics*, **57**, 1444-1452.
- Robein E. and Hanitzsch, C., 2001, Benefits of pre-stack time migration in model building: a case history in the South Caspian Sea: *First Break*, **19**, 183-189.
- Silva, R., and Corcoran, D., 2002, Sub-basalt imaging via pre-stack depth migration – an example from the Slyne Basin, offshore Ireland: *First Break*, **20**, 295-299.
- Spitzer, R., White, R.S., and Christie, P.A.F., 2003, Enhancing sub-basalt reflections using parabolic τ - p transformation: *The Leading Edge*, **22**, 1184-1201.
- Tabti, H., Gelius, L-J., and Hellmann, T., 2004, Fresnel aperture prestack depth migration: *First Break*, **22**, 39-46.
- Theune, U., Sacchi, M. D., and Schmitt, D. R., 2005, Application of local Radon transforms for dip-dependent GPR image decompositions: 75th SEG Ann. Mtg., Houston, 1077-1081.
- Verschuur, D.J., and Berkhout, A.J., 1997, Estimation of multiple scattering by iterative inversion, Part II: Practical aspects and examples: *Geophysics*, **62**, 1596-1611.
- Yilmaz, O., 2001, Seismic data analysis, SEG, Tulsa, OK.

FIGURE CAPTIONS

Figure 1 Location map of the NW Corrib dataset A-1483. A map of water depth is shown. A detailed insert shows the survey geometry (sail lines) and the bathymetry. Colour of the seabed surface insert indicates negative water depth (red and blue colours correspond to shallow and deep parts of the sea floor, respectively). A detailed map of the adjacent Corrib field with the well locations can be found elsewhere (Dancer, 2002).

Figure 2: (a) Input in-line shot gather (after multiple attenuation) and (b) corresponding RMS velocity semblance. Event A is the primary PP wave, event B is the symmetric wave such as P_SP_SP_SP_S, and the group of events C is represented by remnants of free-surface multiples and asymmetric converted (PPSP and PSPP) waves.

Figure 3: RMS velocity semblance panels derived using local moveout operators (Biondi, 1992) for a single in-line shot gather: (a) input data before GDRT, (b) GDRT pass 1 (enhancement of P_SP_SP_SP_S arrivals within the group of events labelled B-C), and (c) GDRT pass 2 (enhancement of PP arrivals). Events H are post-critical arrivals (head waves, diving waves, etc.), event P is the primary PP wave, the group of events B-C is represented by converted waves, events M are remnants of free-surface multiples, and events N are artificial arrivals above 1000 ms that ensure vertical continuity of the inverse GDRT.

Figure 4: Vertical section in the in-line direction of 3D time migrated data (subset 4) after applying the same (PP) time-to-depth vertical stretch for comparison purposes only: (a) PP and (b) symmetric converted wavefields due to GDRT prestack wavefield separation. The difference in apparent dip in the deeper reflectors at the NW end of the line between PP and converted-wave events is a direct consequence of Snell's law: the angle of converted-wave transmission is not equal to the angle of PP-wave transmission. The CDP spacing in the in-line direction is 25 m.

Figure 5: Results of 3D PP time processing (in-line 91, subset 4): (a) focusing of NMO-corrected gathers and (b) focusing of GDRT data. The water replacement velocity is 1578 m/s.

Figure 6: A subset of the initial 3D interval P-wave velocity grid around the target zone. The velocity model is consistent with interpreted key horizons for the 1997 Corrib project and sonic logs acquired in the adjacent area. The volcanics are initially in a single layer confined by the TB and BB horizons. The only lateral heterogeneity allowed at this stage is the variation of the horizon geometries.

Figure 7: PP (top) and PSPPSP (bottom) vertical sections in the in-line direction of 3D depth migrated data after data pre-processing, velocity model building and GDRT wavefield separation (in-line 91, subset 4). The water layer replacement velocity is 1578 m/s. The volcanics are probably in discrete layers and interbedded with the sediments within the overall volcanic wedge. Therefore, at BB it is possible that there is a greater thickness of volcanics hence the large impedance and amplitude contrast. Since the relative strength of the TB and BB horizons is variable, this modifies the earlier statement (Dancer et al., 2005) that the TB horizon has always a stronger impedance contrast when compared to the BB horizon.

Figure 8: Same as in Figure 7, but for vertical PSPPSP sections L1 and L2 corresponding to in-lines 101 and 107 (subset 4). The basin-bounding SW-NE trending fault F1 and the key interpreted horizons SB (seabed), TB (top of basalts), B1 (volcanic unit 1), B2 (volcanic unit 2), BB (base of volcanic sequence), CR (Cretaceous chalk), LM (Bajocian Limestone Marker) and SH (Sherwood Sst. Group) are shown. The cross-line distance is approximately 1 km. Volcanic units 1 and 2 are terminated at the basin-bounding SE-NW trending fault.

Table 1: Some acquisition parameters of the NW Corrib survey A-1483.

Project Code	A-1483
Line Prefix	E021E01
Nominal Fold	60
Recording Length	7168 ms
Sampling Rate	2 ms
Number of cables	8
Number of vessels	1
Cable interval	100 m
Cable length	6000 m
Number of groups	8 x 480
Group interval	12.5 m
Cable depth	12 (+/- 1) m
Source	Sleeve Air guns
Shot interval	25 m
Number of sources	2 (flip-flop)
Source volume	4450 cubic inches
Air pressure	2000 psi
Source depth	12 m
Source separation	50 m

Figure 1

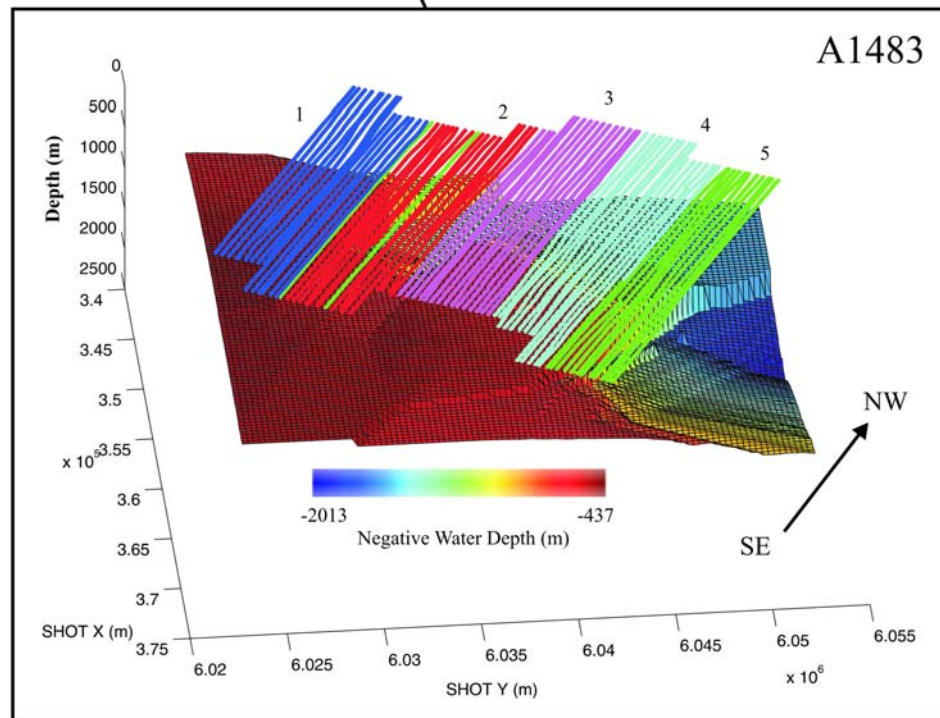
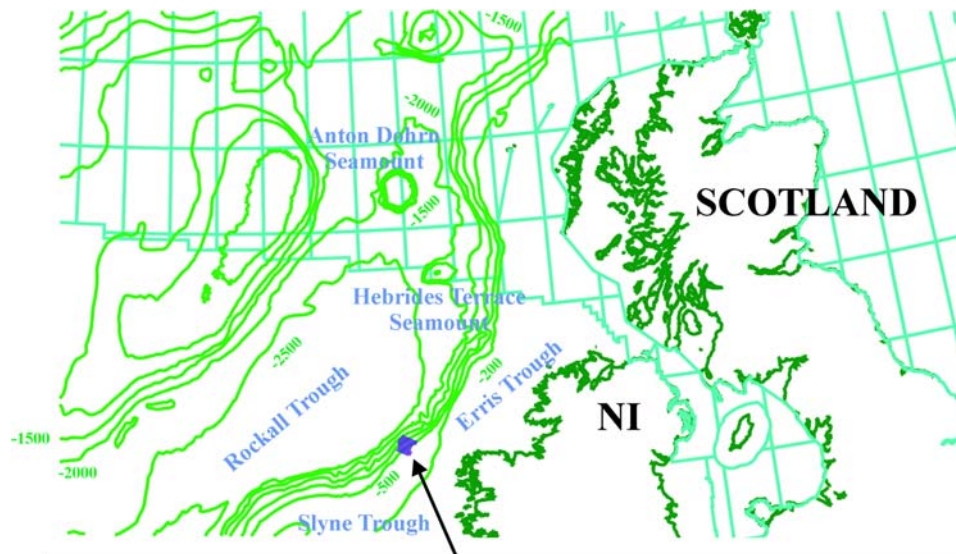


Figure 2

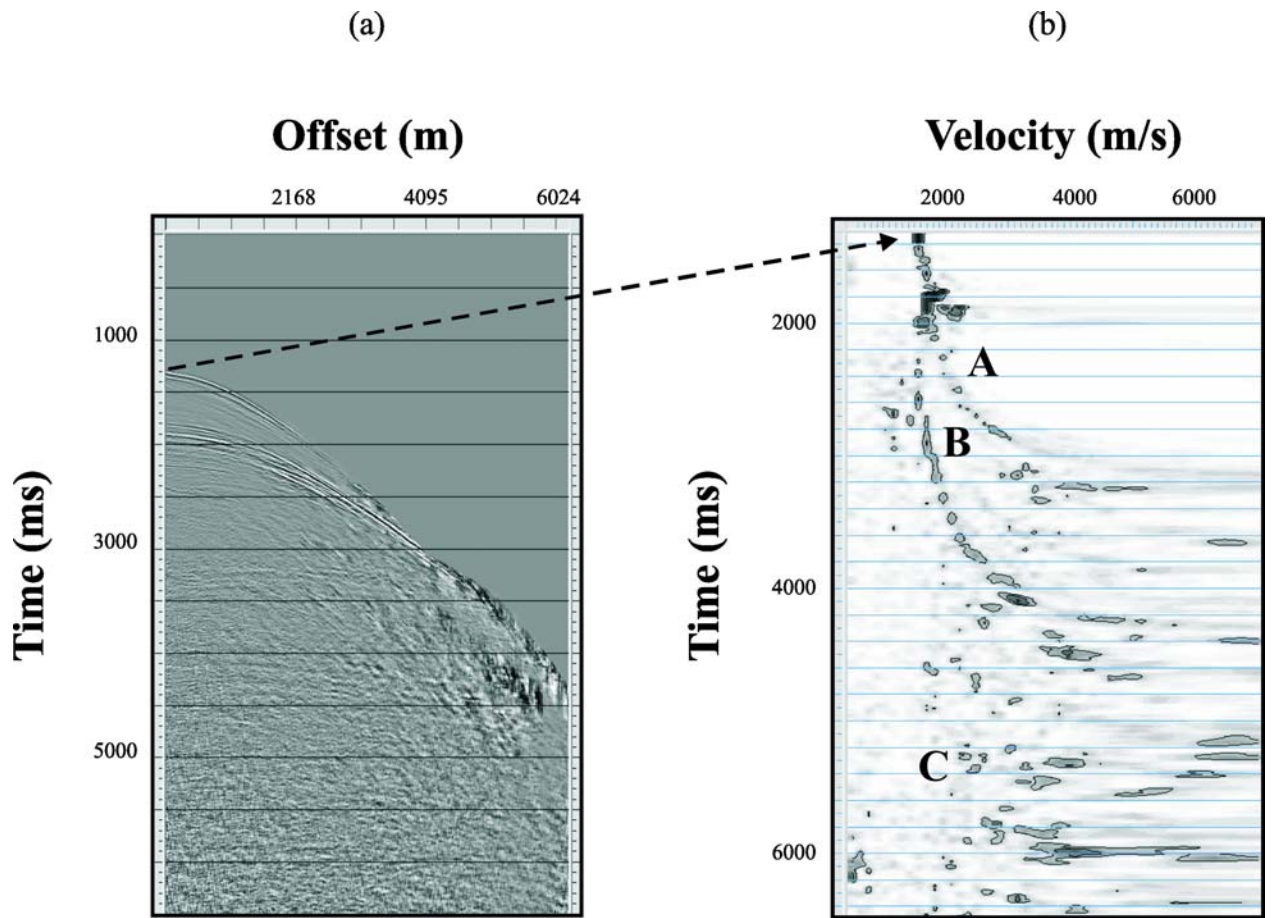


Figure 3

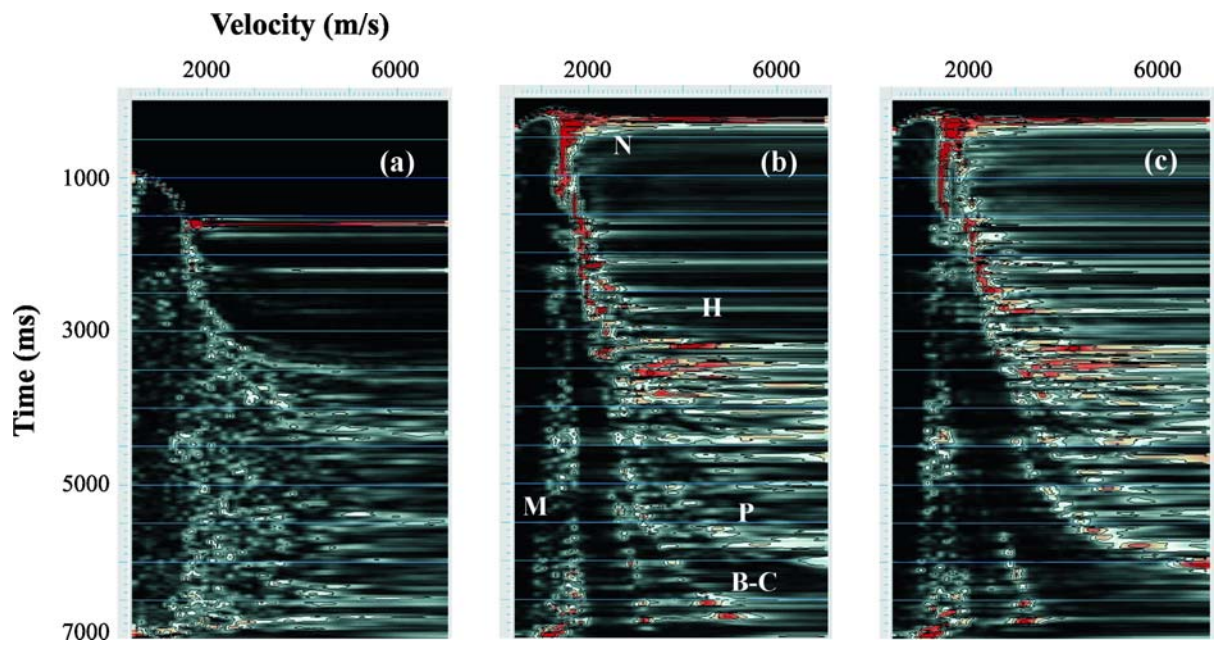


Figure 4

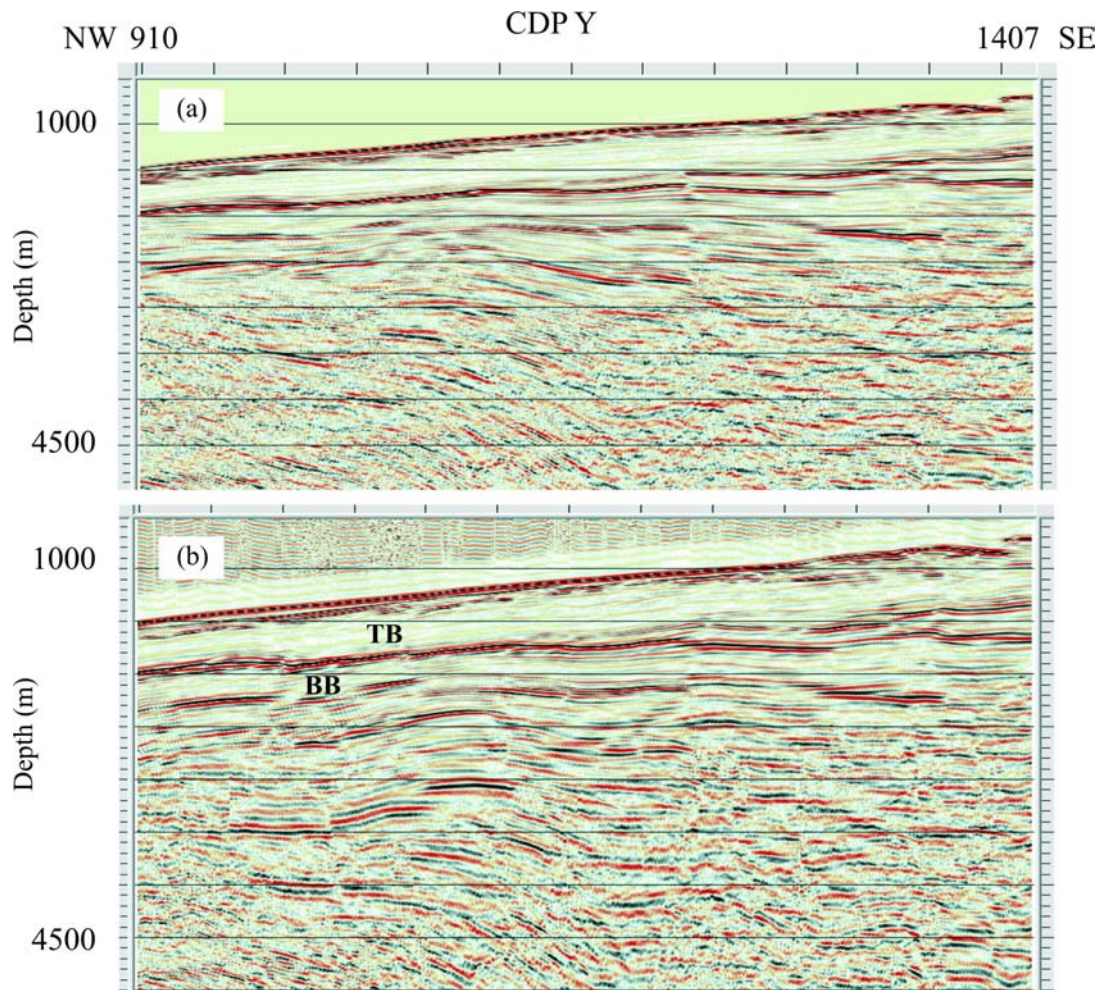


Figure 5

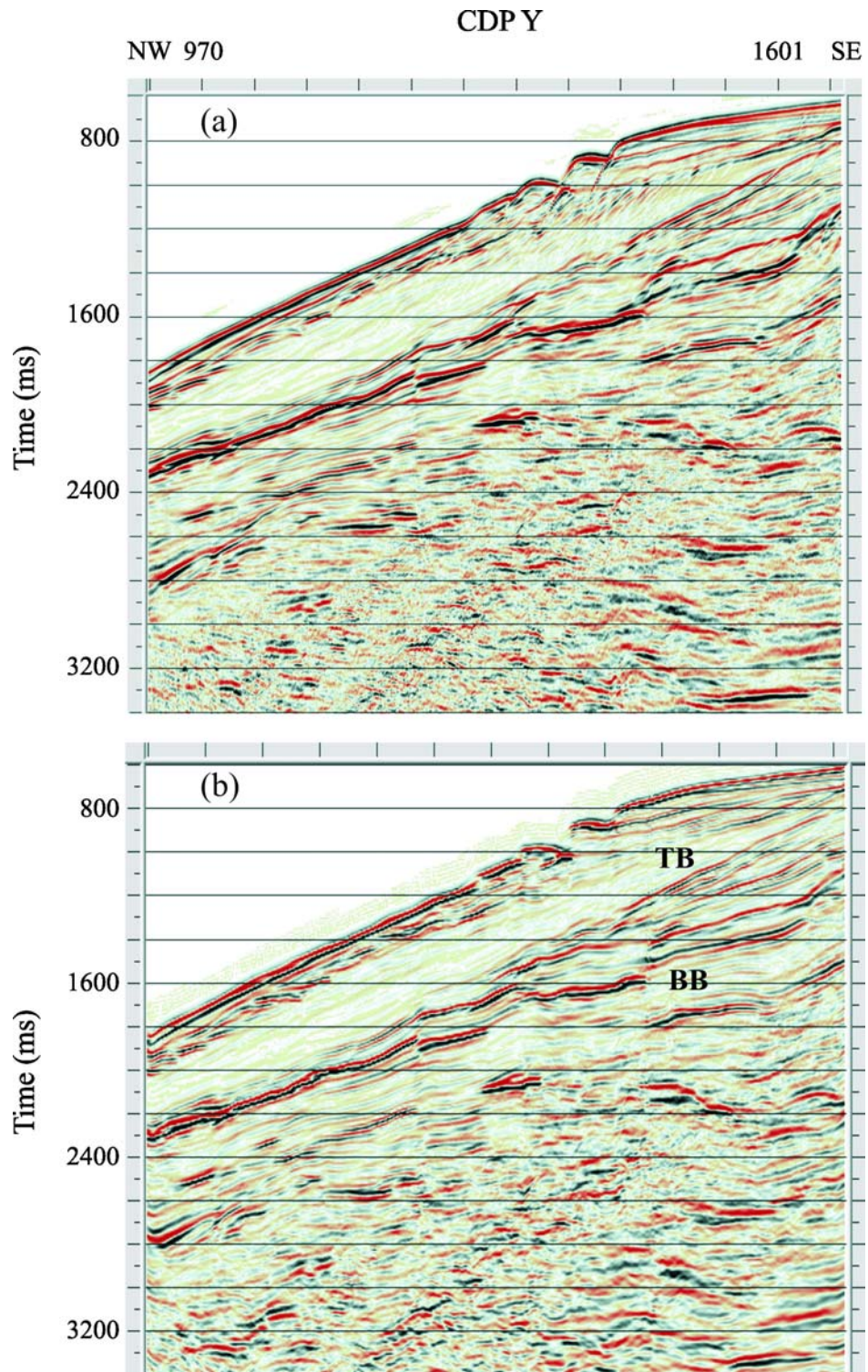


Figure 6

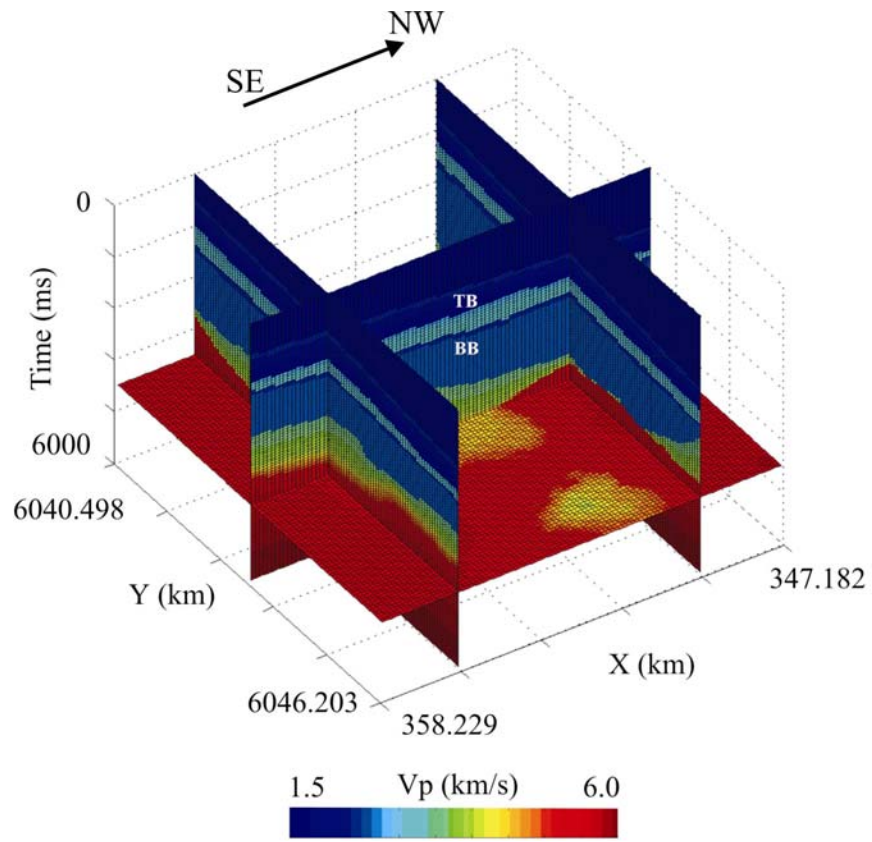
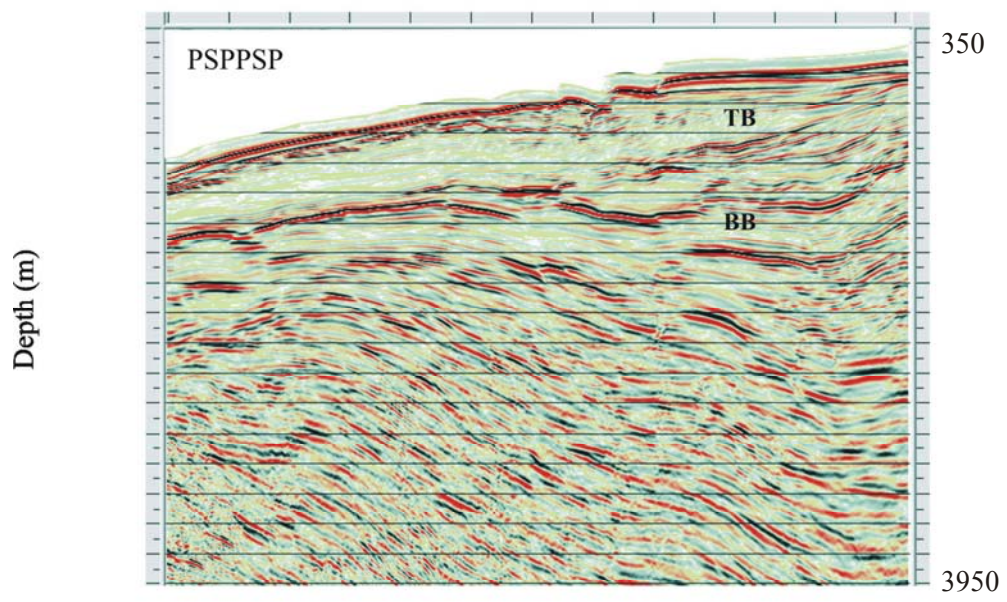
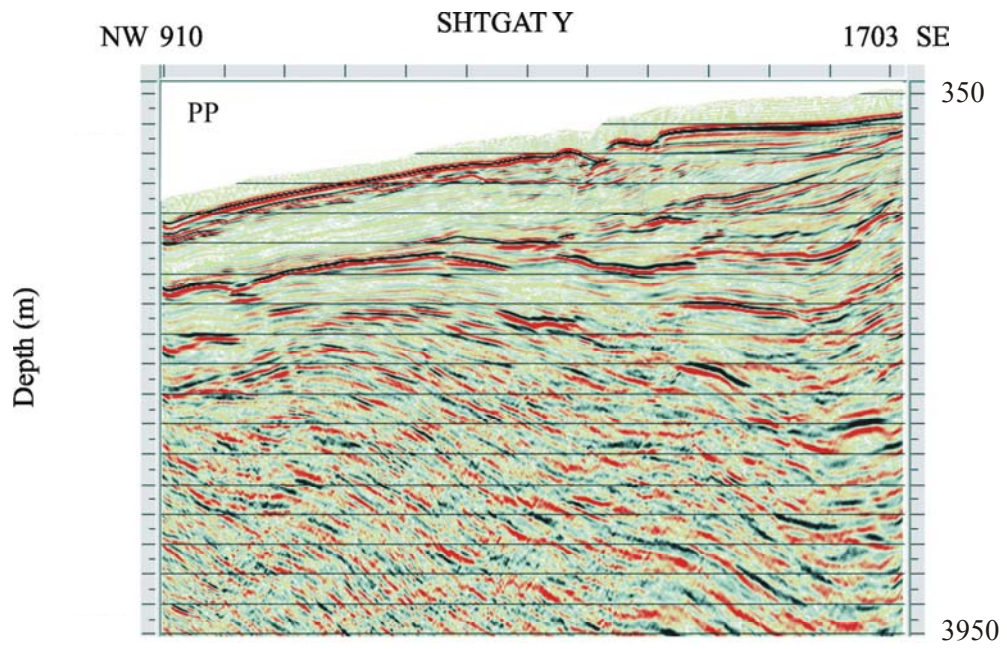


Figure 7



E02IE01-1632-059

Figure 8

